Towards a fast machine-learning-assisted prediction of the mechanoelectric response in organic crystals

Daniele Padula,[a]* Leonardo Barneschi,[a] Andrea Peluso,[b] Tommaso Cinaglia,[a] Alessandro Landi[b†]

[a] *Dipartimento di Biotecnologie, Chimica e Farmacia, Università di Siena, Via A. Moro 2, 53100 Siena, Italy*

[b] *Dipartimento di Chimica e Biologia Adolfo Zambelli, Università di Salerno, Via Giovanni Paolo II, 84084 Fisciano (SA), Italy*

Supporting Information

---

*To whom correspondence should be addressed. Email: daniele.padula@unisi.it

†To whom correspondence should be addressed. Email: alelandi1@unisa.it

Contents

List of Figures

List of Tables

We provide geometries extracted from MD trajectories along with results from DFT simulations and Gromacs topologies ready to run simulations obtained from the Joyce fitting procedure at this public GitHub repository `https://github.com/dpadula85/OFET_strain`.

S1 Computational Details

S1.1 Crystal structures

We retrieved the crystal structure for C10–DNBDT–NW from the Cambridge Structural Database (CSD)[1] (entry 980612).[2]

S1.2 QMD-FF parameterisation

The parameterisation of the QMD-FF for C10–DNBDT–NW occurred by separately fitting parameters for the aromatic core and the C10 side chain, and afterwards joining the two set of parameters with homemade scripts.

In general, the total classical FF representing a target molecule is expressed as the sum of an intra-molecular term E_{FF}^{intra} and an inter-molecular term E_{FF}^{inter}:

$$E_{FF}^{tot} = E_{FF}^{intra} + E_{FF}^{inter} \tag{S1}$$

The inter-molecular term, E_{FF}^{inter}, accounts for the interactions between the target and the surrounding environment, and is usually expressed as a pairwise sum u_{ij}^{inter} between the target's i-th atom and the j-th atom of its embedding, which takes the form:

$$u_{ij}^{inter} = \left(4\varepsilon_{ij}^{inter} \left[\left(\frac{\sigma_{ij}^{inter}}{r_{ij}} \right)^{12} - \left(\frac{\sigma_{ij}^{inter}}{r_{ij}} \right)^{6} \right] \right) + \left(\frac{[q_i q_j]_{inter}}{r_{ij}} \right) \tag{S2}$$

The first term in square brackets on the right side of Eq. S2 is the standard 12-6 Lennard-Jones (LJ) potential, while the second accounts for the Coulomb charge-charge interaction. The LJ parameters were taken from similar atom types described in the OPLS force field,[3] whereas

the point charges have been fitted for each following the RESP procedure[4] on the Molecular Electrostatic Potential generated at same level of theory used for geometry optimisation, including solvation effects through the PCM model.[5]

The intra-molecular term, E_{FF}^{intra}, governs the internal dynamics. We derived the contributions to this term from reference QM data obtained with the GAUSSIAN16 code,[6] for each fragment (either core or side chain). The ground state optimised geometry, Hessian matrix, and vibrational frequencies were obtained at B3LYP-D3/6-31G(d) level including solvation effects through PCM. For rotations around σ bonds in the C10 chain we performed relaxed scans at the same level of theory. We obtained the intramolecular QMD-FF for each fragment using the JOYCE parameterisation protocol.[7–9] We summarise the procedure in four steps:

(i) **assign specific atomic types**

(ii) **assign a suitable set of internal coordinates (ICs)**

(iii) **assign a model potential function to each IC**

(iv) **obtain the intra-molecular parameters (force-constants and equilibrium ICs)**

The selected ICs have been classified in two different sets: stiff or flexible, depending whether rather small displacements from the equilibrium geometry or large amplitude motions are to be expected. Concretely, all possible stretching and bending coordinates were included in the stiff set. Furthermore, several dihedrals, as the one ruling the planarity of the C=C double bonds and their surrounding atoms, were also included in the former set. The dihedrals describing rotations around σ bonds in the C10 chain were instead considered flexible.

When a model potential function is assigned to each selected IC, E^{intra} is therefore further partitioned in several contributions, namely

$$E_{FF}^{intra} = E_s + E_b + E_{st} + E_{ft} + E_{Nb}^{intra} \tag{S3}$$

S5

The first three terms refer to stiff IC, and can be approximated through harmonic potentials, *i.e.*

$$E_s = \frac{1}{2}\sum_s^{N_s} k_s(r - r^0)^2 \; ; \; E_b = \frac{1}{2}\sum_b^{N_b} k_b(\theta - \theta^0)^2 \; ; \; E_{st} = \frac{1}{2}\sum_{st}^{N_{st}} k_{st}(\phi - \phi^0)^2 \tag{S4}$$

The stretching and bending contributions, E_s and E_b, are widely used by popular FFs. The third expression (E_{st}) is seldom employed to describe torsions of stiff dihedral angles in standard approaches. Yet, it appears to be better suited to account for the internal energy due to small and fast distortions of a dihedral ϕ from its equilibrium position ϕ^0. The JOYCE procedure routinely employs the E_{st} term, to mimic the behaviour of a stiff and fast vibrating torsion, as those ruling the planarity of aromatic rings or conjugated double bonds. [7,10] The second-to-last term of Eq. S3 refers to flexible ICs, expected to experience larger distortions during simulation. In fact, the term

$$E_{ft} = \sum_\mu^{N_{ft}} \sum_j^{N_{cos\mu}} k_{j\mu}^{ft}\left[1 + cos(n_j^\mu \delta_\mu - \gamma_j^\mu)\right] \tag{S5}$$

(where δ_μ is the μ-th flexible torsion, $k_{j\mu}^{st}$ its force constant, n_j^μ the multiplicity and γ_j^μ a proper phase), is devised to describe large amplitude displacements induced by a flexible dihedral, *e.g.* a rotation around a σ bond. The last term of Eq. S3, contains the non-bonded intra-molecular interactions, implemented, similarly to the inter-molecular term (Eq. S2), as a sum of electrostatic charge-charge and Lennard-Jones (LJ) terms, expressed as

$$E_{Nb}^{intra} = \sum_i \sum_{i<j} \frac{q_i^{intra} q_j^{intra}}{r_{ij}} + \sum_i \sum_{i<j} 4\varepsilon_{ij}^{intra}\left[\left(\frac{\sigma_{ij}^{intra}}{r_{ij}}\right)^{12} - \left(\frac{\sigma_{ij}^{intra}}{r_{ij}}\right)^6\right] \tag{S6}$$

Although ε^{intra} and σ^{intra} can in principle assume different values with respect to ε^{inter} and σ^{inter}, in most popular transferable FFs the non-bonded contributions are counted among all possible pairs of interacting sites i-j, adopting the same set of LJ and charge parameters for both inter-molecular and intra-molecular interactions. Additionally, one may decide to only parameterise the intra-molecular part of the force field, to describe the internal dynamics of the chromophore,

S6

or also the inter-molecular part, which affects distances and stacking between different molecules. While both are important for the problem at hand, we limited the parameterisation to the intra-molecular part,[10] resorting to inter-molecular parameters taken from the OPLS force field,[3] similarly to what done in unrelated studies.[10,11]

Once the FF functional form and the underlying IC's collection have been selected, step (iv) can be accomplished and a complete set of QMD-FF parameters eventually retrieved by minimising the functional

$$I^{intra} = \sum_{K \leq L}^{3N-6} \frac{2W_{KL}''}{C} \left[H_{KL} - \left(\frac{\partial^2 E_{FF}^{intra}}{\partial Q_K \partial Q_L} \right) \right]_{g_0}^2 + \sum_{g}^{N_{geom}} W_g \left[\Delta U_g - E_g^{intra} \right]^2 \qquad (S7)$$

In the first term on the right side of Eq. S7 the sum runs over the 3N-6 dye's coordinates, C is a normalization factor, Q_K is the Kth normal mode, whereas H_{KL} and $\frac{\partial^2 E^{intra}}{\partial Q_K \partial Q_L}$ are QM and FF Hessian matrix elements, both evaluated in the minimum energy geometry (g_0). The normalised diagonal elements of the weight matrix $\mathbf{W}''$ are set at twice the value of those corresponding to the off diagonal terms. In the second term, ΔU_g is the QM computed energy difference between the the g and g_0 geometries and N_{geom} is the number of the different geometrical arrangements sampled for each target molecule. The weights W_g are all initially set the same value.

Finally, we obtained the total FF for C10–DNBDT–NW replacing hydrogen atoms in the previously parameterised FF for the π–conjugated core with alkyl side chains of the appropriate length. The topology merge was carried out with home made scripts, and missing stretching, bending, and torsional terms were added by hand using parameters transferred from the alkyl side chain parameterisation. We introduced intramolecular LJ terms among side chains and between core and chains, to avoid undesired proximity. We fitted point charges, according to the RESP procedure,[4] to the B3LYP-D3/6-31G(d) electrostatic potential of the entire molecule.

Table S1: Number of internal coordinates and standard deviation of the QMD-FFs fitting procedure.

Fragment	IC	σ / kJ mol^{-1}
core	217	0.005
chain	139	0.057

Table S2: RMSD between QM and MM optimised geometries in terms of bond lengths, bending angle, dihedrals and molecular normal modes (total) for C10–DNBDT–NW.

Bond lengths / Å	Bending angles / deg	Dihedrals / deg	Total / Å
0.000	0.077	1.302	0.050
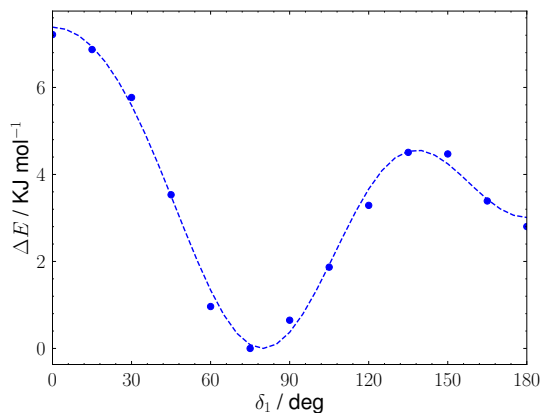
Fig. S1: QM (dots) and MM (dashed lines) potential energy profiles for the dihedral angle between the π–conjugates moiety and the alkyl substituent for C10–DNBDT–NW.

S1.3   MD simulations

We ran classical MD simulations on crystals with the GROMACS 2020.5 software.[12] We generated a $1 \times 5 \times 19$ supercell containing 190 molecules in total (19380 atoms). We adopted periodic boundary conditions taking into account long range electrostatic effects through the PME algorithm.[13] We used an integration time step of 1 fs, imposing contraints on all bonds through the LINCS algorithm,[14] adopting a Berendsen thermostat to control temperature.[15]

The computational protocol consisted of an initial steepest descent minimisation, followed by a slow NVT heating procedure starting from 25 K, initially carried out keeping aromatic cores frozen, and gradually releasing them at 300 K. After equilibrating the system at the target temperature in NVT conditions for 2 ns, we carried out a production run in NVT conditions, for 10 ns. The last 5 ns of this trajectory were used to evaluate properties at $\varepsilon = 0$.

To evaluate electronic properties at various strain values, we started from the last step described above, and ran analogous 20 ns production simulations, this time imposing LINCS constraints only on bonds involving hydrogen atoms, and switching temperature to Bussi thermostat. [16] Before restarting the run, we reduced (for $\varepsilon < 0$, or increased for $\varepsilon > 0$) the box size by 0.5%, and then restarted the trajectory in the same conditions (NVT) for 20 ns. We repeated this procedure for each value of ε in steps of 0.5%, until a maximum strain of $\varepsilon = \pm 3\%$ was reached. We used the last 10 ns to evaluate electronic couplings between pairs of molecules and their fluctuations, extracting snapshots every 50 ps. To evaluate spectral densities, we ran, for each value of ε, a short 10 ps trajectory, extracting snapshots every 10 fs.

All MD trajectories were processed and analysed with Gromacs tools and exploiting the MD-Analysis python library [17–21] in homemade scripts.

S1.4 Electronic calculations

Unless stated otherwise, we performed all quantum chemical calculations with the Gaussian16 software, [6] adopting B3LYP as functional including Grimme's D3 dispersion correction, [22] and 6-31G* as basis set, for a direct comparison with previously published data. [2] All calculations took into account environmental polarisation effects through the PCM model ($\epsilon_{PCM} = 4$). [10,23,24] For the evaluation of hole transport properties we performed geometry optimisations, frequency and single point calculations in both the neutral and positively charged ($q = +1$) state. We computed hole transfer integrals between frontier orbitals as $J_{ij} = \langle \phi_i | \hat{F} | \phi_j \rangle$, where ϕ_i and ϕ_j are the unperturbed HOMO orbitals of the isolated monomers, respectively, and $\hat{F}$ is the Fock operator of the dimer. [10,25–27] Snapshots extracted from all trajectories were processed by cropping side

chains after the first carbon atom, so as to leave the aromatic core substituted with methyl groups, in analogy to our previous work and to what similarly done by others, [10,28–30] before running electronic calculations at B3LYP-D3/6-31G* level, including environmental polarisation effects through the PCM model ($\epsilon_{PCM} = 4$).[24]

S1.5 Crystal phonons

It is widely known that the computation of crystal phonons is an extremely time-consuming process.[27,31] To develop a method that can be used as a predictive tool for the analysis of new materials, we here lower the computational burden by resorting to the self-consistent charge density functional tight-binding(SCC-DFTB) method as implemented in the DFTB+ software package.[32,33] DFTB is a nonorthogonal tight-binding method based on a second-order expansion of the DFT total-energy expression, which leads to computations about 3-4 orders of magnitude faster than DFT.

The 3-ob-1 Slater-Koster set parameters have been employed for the molecule under study.[34,35] The atomic positions of the unit cell have been optimized keeping the experimental lattice values fixed, using the conjugate gradient method with a force-threshold criterion of 10^{-8} Hartree per Bohr radius. We have used periodic boundary conditions employing a $1 \times 2 \times 2$ Monkhorst-Pack k-point sampling scheme.[36] The Lennard-Jones dispersions[37] have been included to take into account the weak van der Waals interaction in the crystalline phase.

To investigate the phonon dispersion relations in crystalline phases, we have employed the frozen phonon calculation in which the sampling of the q-space relies on calculation of second derivatives of the energy on sufficiently large supercells. In line with what has been done in previous works,[27,38,39] a 1x2x2 supercell has been used in order to have larger dimension for the high-mobility (b, c) plane. These calculations have been carried employing a 1x1x1 k-point sampling Monkhorst-Pack scheme.

S1.6 Hole mobility calculations

S1.6.1 Fermi's Golden Rule

We evaluated rate constants by first order time-dependent perturbation theory, Fermi's Golden Rule (FGR), following Eq. 1 reported in the main text, where the FCWD $F(\Delta E_{ij}, T)$ is defined as:

$$F(\Delta E_{ij}, T) = \frac{1}{Z} \sum_{v_i, v_j} \mathrm{e}^{-\beta E_{v_i}} |\langle v_i | v_j \rangle|^2 \delta(E_{v_i} - E_{v_j} - \Delta E_{ij}) \tag{S8}$$

where $\langle v_i | v_j \rangle$ is the Franck-Condon integral, Z is the vibrational partition function of the initial electronic state, $\beta = 1/(k_\mathrm{B}T)$, and the sum runs over all vibrational states of $|i\rangle$ and $|j\rangle$.

Here, we have adopted the generating function (GF) approach for the evaluation of $F(\Delta E_{ij}, T)$,[40,41] which, in the framework of harmonic approximation for nuclear motions, allows to compute $F(\Delta E_{ij}, T)$ considering the whole set of the normal modes of both initial and final states, taking into account effects due to both changes of the equilibrium positions and of vibrational frequencies, as well as the effects due to normal mode mixing. The GF approach allows to handle the infinite summations appearing in Eq. S8 exploiting the integral representation of Dirac's delta function and Duschinsky's normal mode transformation:[42]

$$\mathbf{Q}_i = \mathbf{J}\mathbf{Q}_j + \mathbf{K} \tag{S9}$$

where $\mathbf{J}$ and $\mathbf{K}$ are the rotation matrix and the equilibrium displacement vector, respectively, while $\mathbf{Q}_i$ and $\mathbf{Q}_j$ are the normal coordinates of the electronic states $|i\rangle$ and $|j\rangle$.

We obtained Franck-Condon weighted densities of states (FCWDs) using a development version of the MolFC package,[43] using DFT/B3LYP-D3/6-31G(d) for geometry optimisations and normal modes analyses. We adopted the curvilinear coordinate representation of normal modes, to prevent that large displacements of a angular coordinates could reflect into large shifts from the equilibrium positions of the involved coordinate. Such unphysical effect is unavoidable when using rectilinear coordinates and requires the use of high order anharmonic potentials for its

correction.[44]

S1.6.2 Transient Localisation Theory

According to transient localisation theory (TLT), the effects of dynamic disorder can be monitored by a transient localisation over a length L within a fluctuation time scale given by the inverse of the typical intermolecular oscillation frequency $\tau = 1/\omega_0$:

$$\mu = \frac{e}{k_{\mathrm{B}}T} \frac{L^2(\tau)}{2\tau}, \tag{S10}$$

In this work, a typical value $(\tau = 1 \text{ ps})$[45] for the intermolecular oscillation time is assumed for all the molecules; nevertheless, the dependence of the mobility on the molecular fluctuation time is weak,[45] so that different τ in a realistic range $[0.1; 100]$ ps would lead to very similar μ values.[45]

As described in greater details in ref.s 46 and 47, this method can be summarised in the following steps:

1. Define the supercell of the system, that is, the positions of all molecular sites in presence of periodic boundary conditions. Obviously, the supercell must be larger than the $L(\tau)$ reached by the moving charge. This can be obtained by checking convergence for different system sizes.

2. Evaluate the oscillations of the transfer integral σ for all the interacting couples in the crystal.

3. Build a disordered Hamiltonian of the size of the supercell displaying off-diagonal disorder given by the oscillations σ

4. Diagonalize the Hamiltonian to calculate $L(\tau)$

5. Repeat steps 2-4 several times with different realisations of disorder (to take into account the random nature of the disorder in real systems) and compute average $L(\tau)$. The statistical

error on $L(\tau)$ can be made arbitrarily small by increasing the number of realizations.

6. Evaluate the mobility through Eq. S10

S1.6.3 Kinetic Monte Carlo

We carried out kMC simulations at each value of strain on snapshots extracted from classical MD trajectories at that value of strain. Since boxes from classical MD simulations are too small to perform statistically meaningful simulations, we combined 200 snapshots in a mesoscopic lattice, as described in ref. 48. For each snapshot we computed transfer integrals with our ML model, using the centres of mass of the molecules as sites in the kMC simulations: the simulation is thus "*quasi* 2D", because the centres of mass approximately lie on the (b, c) plane. The mesoscopic lattice is created by combining the 200 snapshots extracted from classical MD trajectories in a $b \times c$ 10×20 grid,[48] because c is the main transport axis. Note that this grid refers to MD simulation boxes, which are $1 \times 5 \times 19$ supercells. The kMC mesoscopic lattice thus has the final dimensions of $50b \times 380c$, with respect to the crystallographic unit cell. Each kMC trajectory is propagated by randomly placing the hole in the box, and allowing hopping to one of the nearest neighbours as the only possible process at each time step. The hopping rate k_{ij} between sites i and j is computed on-the-fly according to Fermi's Golden Rule (FGR) given the value of the transfer integral J_{ij} previously computed through the ML model and the Franck–Condon Weighted Density of States (FCWD, $F(\Delta E_{ij}, T)$) previously computed through geometry optimisation and frequency calculations on the neutral and charged states.

S2 Structural Analyses

Since the distance between monomers r is not the only factor affecting transfer integrals J, but also the relative orientation plays a role, we have performed further analyses to find the rationale behind the apparently irregular behaviour of transfer integral J_2.
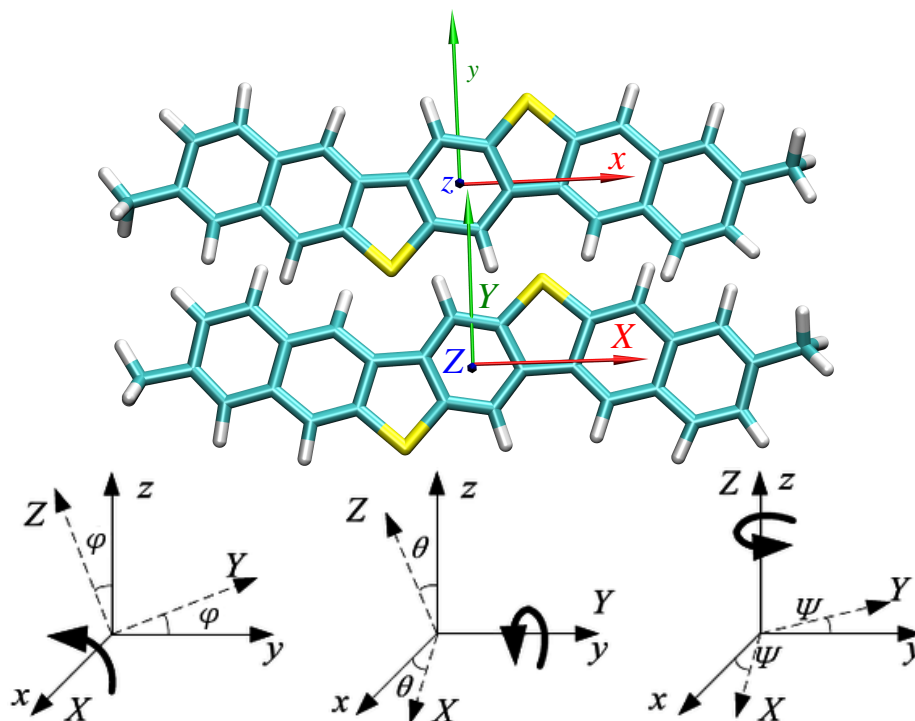
Fig. S2: Local reference frames (top) and definition of Euler angles (bottom) used for the structural analyses reported in this section.

We defined a local reference frame on each monomer (see Fig. S2) constituting the dimer for which we computed J_2 at DFT level:

1. we obtained the least squares plane passing through all atoms in the π–conjugated moiety, defining the normal to this plane as the local z axis;

2. the local reference frame has its origin in the projection of the centre of mass onto the least squares plane;

3. the long molecular axis x is chosen such that it passes through the projections of substituted carbon atoms of the π–conjugated core onto the least squares plane;

4. the short molecular axis y is obtained from the cross product of the other two axes: $y = z \times x$, to define a right-handed reference frame.

Once the two reference frames have been defined, the unit vectors are collected in the columns of two matrices, R_1 and R_2. The relative orientation of the two monomers is then described by the Euler angles associated to the transformation matrix $U = R_2 R_1^{-1}$ that transforms the reference frame R_1 onto reference frame R_2. If we consider the two monomers as rigid bodies, Euler angles represent a relative motion named: (i) roll, for rotation around x (angle ϕ); (ii) pitch, for rotation around y (angle θ); (iii) yaw, for rotation around z (angle ψ).

S2.1 Strain along c

In Table S3 we report the average value of each angle, as well as its standard deviation, obtained from MD simulations for strain along the c axis.

Table S3: Orientation analysis for strain along c.

ε / %	J_1			J_2		
	ϕ / °	θ / °	ψ / °	ϕ / °	θ / °	ψ / °
−3.0	-0.02 ± 1.90	0.13 ± 4.25	-0.48 ± 4.12	-8.12 ± 2.78	14.55 ± 4.07	-10.37 ± 3.95
−2.5	-0.01 ± 1.95	0.05 ± 4.14	-0.27 ± 4.14	-8.37 ± 2.78	15.18 ± 4.03	-10.04 ± 3.68
−2.0	0.13 ± 1.86	-0.43 ± 3.73	-0.12 ± 4.14	-8.72 ± 3.13	15.66 ± 4.45	-10.28 ± 4.21
−1.5	-0.10 ± 2.09	0.45 ± 4.27	-0.50 ± 4.47	-8.62 ± 3.26	15.60 ± 4.54	-10.49 ± 4.35
−1.0	-0.11 ± 2.05	-0.18 ± 4.14	-0.40 ± 4.11	-8.55 ± 3.21	15.70 ± 4.80	-10.16 ± 4.17
−0.5	0.28 ± 2.11	-0.61 ± 4.68	0.20 ± 4.56	-8.28 ± 3.06	15.69 ± 4.62	-10.11 ± 3.89
0.0	0.21 ± 1.99	0.04 ± 4.08	1.04 ± 3.56	-8.37 ± 2.73	16.18 ± 3.77	-9.61 ± 3.96
1.0	0.13 ± 2.29	-0.30 ± 4.50	-0.03 ± 3.95	-8.06 ± 3.02	15.49 ± 4.44	-10.19 ± 4.38
1.5	0.20 ± 2.24	-0.47 ± 5.02	-0.07 ± 4.61	-8.13 ± 3.33	15.37 ± 5.15	-10.29 ± 4.73
2.0	0.19 ± 2.20	-0.53 ± 5.12	-0.20 ± 4.21	-8.10 ± 3.42	15.99 ± 5.11	-11.56 ± 4.31
2.5	-0.59 ± 2.38	-1.38 ± 5.05	0.18 ± 4.27	-7.12 ± 3.32	9.61 ± 6.41	-8.69 ± 4.20
3.0	-0.27 ± 2.40	0.14 ± 5.09	-0.16 ± 4.39	-7.10 ± 3.41	7.18 ± 5.61	-9.46 ± 4.39

From Table S3 we highlight that, for the pair of monomers giving rise to J_1, the relative orientation remains approximately the same. However, for the pairs of monomers giving rise to J_2, we notice that for $\varepsilon > 2\%$ Euler angles slightly decrease: for ϕ and ψ it is difficult to say whether this reduction is statistically significant, since it is rather modest. On the other side, for θ the reduction is significant, and it brings the two monomers in a more parallel arrangement, which favours electronic interactions between frontier orbitals. Since this analysis is based on a rigid body approximation, which may not be appropriate for molecules, we tried to understand whether

this is a feature of the specific pair of monomers that we picked for DFT computations, or whether this feature is present for all pairs giving rise to a J_2 transfer integral. In Table S4, we report the results of these structural analyses for all pairs of monomers in the aggregate.

Table S4: Aggregate orientation analysis for strain along c.

ε / %	J_1			J_2		
	ϕ / °	θ / °	ψ / °	ϕ / °	θ / °	ψ / °
−3.0	0.00 ± 2.06	0.01 ± 3.58	0.00 ± 3.66	1.10 ± 7.24	15.77 ± 4.33	-8.75 ± 4.07
−2.5	-0.01 ± 2.11	0.01 ± 3.68	-0.01 ± 3.69	1.07 ± 7.22	15.94 ± 4.40	-8.78 ± 4.10
−2.0	-0.01 ± 2.14	0.01 ± 3.79	-0.01 ± 3.76	1.08 ± 7.28	16.22 ± 4.51	-8.77 ± 4.18
−1.5	0.00 ± 2.16	-0.01 ± 3.81	-0.01 ± 3.77	1.05 ± 7.21	16.17 ± 4.59	-8.79 ± 4.19
−1.0	-0.01 ± 2.18	-0.01 ± 3.90	-0.03 ± 3.83	1.02 ± 7.19	16.27 ± 4.69	-8.80 ± 4.24
−0.5	-0.01 ± 2.19	0.00 ± 3.95	0.01 ± 3.88	1.02 ± 7.17	16.39 ± 4.72	-8.80 ± 4.32
0.0	0.01 ± 2.24	0.01 ± 4.06	-0.01 ± 3.98	0.99 ± 7.18	16.52 ± 4.82	-8.80 ± 4.38
1.0	-0.01 ± 2.30	0.01 ± 4.18	0.00 ± 4.04	0.95 ± 7.10	16.52 ± 5.04	-8.80 ± 4.49
1.5	0.00 ± 2.37	0.03 ± 4.35	0.01 ± 4.15	0.94 ± 7.07	16.50 ± 5.20	-8.79 ± 4.58
2.0	-0.02 ± 2.53	0.01 ± 4.47	-0.01 ± 4.11	1.08 ± 6.98	14.32 ± 6.34	-8.59 ± 4.58
2.5	-0.03 ± 2.56	0.03 ± 4.55	-0.04 ± 4.17	1.05 ± 6.94	14.16 ± 6.52	-8.67 ± 4.63
3.0	0.00 ± 2.59	0.01 ± 4.62	-0.01 ± 4.24	1.05 ± 6.90	14.06 ± 6.75	-8.63 ± 4.68

In Table S4 it is clear that the orientational behaviour of pairs of monomers is different when averaged over all the aggregate, confirming that the pair chosen for the DFT computation of J_2 shows a structural behaviour that is peculiar and deviating from average. It is evident that better statistical sampling would thus yield a more regular behaviour for J_2, as we observe for the data originating from the ML model.

S2.2 Strain along b

In Table S5 we report the average value of each angle, as well as its standard deviation, obtained from MD simulations for strain along the b axis.

Table S5: Orientation analysis for strain along b.

ε / %	J_1			J_2		
	ϕ / °	θ / °	ψ / °	ϕ / °	θ / °	ψ / °
−3.0	-0.13 ± 1.98	0.35 ± 4.33	0.24 ± 3.98	-8.61 ± 2.92	16.81 ± 4.36	-10.26 ± 3.66
−2.0	-0.09 ± 2.03	0.06 ± 4.52	0.12 ± 3.80	-8.62 ± 3.17	16.31 ± 4.63	-10.74 ± 4.16
−1.0	-0.05 ± 1.99	-0.12 ± 4.68	0.09 ± 4.57	-8.30 ± 3.06	15.88 ± 4.74	-10.31 ± 4.21
0.0	0.21 ± 1.99	0.04 ± 4.08	1.04 ± 3.56	-8.37 ± 2.73	16.18 ± 3.77	-9.61 ± 3.96
1.0	0.04 ± 2.46	0.14 ± 5.17	0.44 ± 4.70	-8.31 ± 3.53	15.49 ± 5.11	-9.96 ± 4.81
2.0	0.11 ± 2.21	-0.27 ± 4.90	0.07 ± 4.63	-8.37 ± 3.24	15.26 ± 4.83	-10.17 ± 4.54
3.0	0.24 ± 2.76	0.82 ± 4.60	-0.28 ± 5.01	-7.94 ± 3.15	10.49 ± 4.97	-8.96 ± 4.79

Also in this case, for the pairs of monomers giving rise to J_2, we notice that for $\varepsilon > 2\%$ Euler angles slightly decrease, with a significant reduction especially for θ. In Table S6, we report the results of these structural analyses for all pairs of monomers in the aggregate.

Table S6: Aggregate orientation analysis for strain along b.

ε / %	J_1			J_2		
	ϕ / °	θ / °	ψ / °	ϕ / °	θ / °	ψ / °
−3.0	-0.01 ± 2.03	0.00 ± 3.92	-0.01 ± 3.45	0.87 ± 6.78	16.58 ± 4.67	-8.88 ± 3.87
−2.0	-0.01 ± 2.10	-0.01 ± 3.95	-0.02 ± 3.63	0.90 ± 6.93	16.59 ± 4.71	-8.83 ± 4.08
−1.0	0.00 ± 2.18	0.01 ± 4.01	-0.01 ± 3.78	0.93 ± 7.01	16.48 ± 4.78	-8.83 ± 4.18
0.0	0.01 ± 2.24	0.01 ± 4.06	-0.01 ± 3.98	0.99 ± 7.18	16.52 ± 4.82	-8.80 ± 4.38
1.0	-0.01 ± 2.33	0.00 ± 4.10	0.00 ± 4.15	1.02 ± 7.26	16.31 ± 4.91	-8.75 ± 4.58
2.0	0.00 ± 2.41	0.01 ± 4.18	-0.01 ± 4.32	1.05 ± 7.29	16.05 ± 5.03	-8.73 ± 4.75
3.0	0.03 ± 2.56	-0.02 ± 4.29	0.00 ± 4.48	1.22 ± 7.38	14.27 ± 5.90	-8.58 ± 4.92

Also in this case the orientational behaviour of pairs of monomers is different when averaged over all the aggregate, confirming that the pair chosen for the DFT computation of J_2 shows a peculiar structural behaviour, and that the irregular pattern observed in Fig 2 could be better characterised with a larger statistical sampling for DFT data, possibly providing a behaviour similar to what obtained with the ML model.

S3 Machine Learning models

We trained and evaluated ML models exploiting the Scikit-learn python library[49] in homemade scripts. The Coulomb matrix elements $\mathbf{C}_{ij}$ are defined as

$$\mathbf{C}_{ij} = \begin{cases} 0.5Z_i^{2.4}, & i = j \\ \dfrac{Z_i Z_j}{r_{ij}}, & i \neq j \end{cases} \tag{S11}$$

This description was introduced to provide a rotationally and translationally invariant representation of molecules that would require as input the same data used for typical quantum chemical calculations,[50] *i.e.* atomic numbers and coordinates. We can thus represent a dimer through a Coulomb matrix. The Coulomb matrix can be reordered such that atoms belonging to each monomer are consecutive, so that it will be constituted by four blocks:[51,52] two different intra-molecular blocks (on the diagonal), which are the Coulomb matrices of the monomers, and two inter-molecular blocks, which depend on distances r_{ij} between pairs of atoms belonging to two different monomers. Since it is well known that transfer integrals are mostly affected by inter-molecular motions,[53] to reduce the number of parameters of the ML model to avoid overfitting it is possible to use as input to the ML model only one of the two equivalent off-diagonal inter-molecular blocks of the Coulomb matrix. Thanks to this strategy described by Wang,[51] great performances in terms of errors and speed were achieved in the calculation of transfer integrals for case-study molecules,[51] even exploring the effect of various algorithms.[52] Since our training set size is limited to ≈ 10000 DFT evaluations, using a smaller input size allows reducing the parameters of the ML models, thus limiting the possibility of overfitting.

We used the intermolecular portion of the Coulomb matrix as input for various ML models, namely k–Nearest Neighbours (KNN, $k = 13$), Kernel Ridge Regression (KRR) with either Laplacian or Gaussian (Radial Basis Functions, RBF) kernel, Lasso Regression, and Random Forest. The best hyperparameters for each model were identified minimising the average cross-validation RMSE with a grid search and a K-Fold ($K = 5$) cross-validation scheme. The bounds for the various

hyperparameters of each model are reported in Table S7.

Table S7: Hyperparameter tuning for Machine Learning models used in this study.

Model	H_1			H_2			H_3		
	name	range	opt	name	range	opt	name	range	opt
KNN	metric	mi, eu, ma[a]	mi	dist	uni, w[b]	uni	k	] 0, 20]	13
KRR-LAPL	α	[1e−4, 1e3]	0	γ	[1e−4, 1e3]	1e−3			
LASSO	α	[1e−4, 1e3]	1e−3						
KRR-RBF	α	[1e−4, 1e3]	1e−4	γ	[1e−4, 1e3]	1e−4			

[a] mi: Minkowski distance, eu: Euclidean distance, ma: Manhattan distance

[b] uni: uniform, w: weighted

In a first screening of models, we identified KRR-RBF as the model with the lowest cross-validation error, but it yields some predictions that are negative, a feature that we attributed to its non-linearity. Since the training was conducted on the absolute value of the transfer integral $|J|$, thus no negative predictions are expected, we decided not to use this model itself, but rather to combine it with the second best model, the Random Forest one, in a stacked estimator. A stacked estimator is yet another Machine Learning model that learns how to combine the predictions of several other models to minimise the error. The resulting stacked model yields predictions that are comparable, in terms of error, to the ones obtained with the KRR-RBF model, but it does not produce any negative value of the transfer integral.
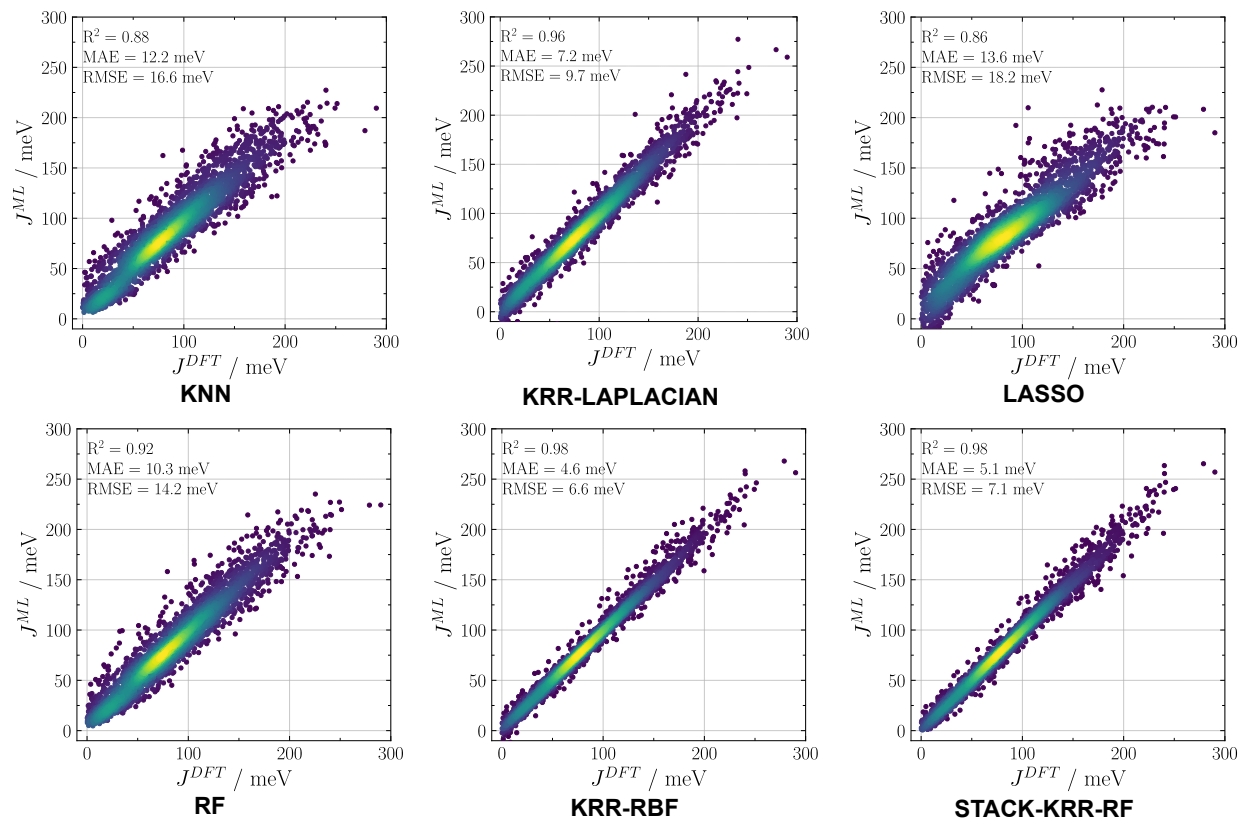
Fig. S3: Correlation between transfer integrals computed with DFT and various ML models on the test set (30% of the total data, ≈ 3000 points).

The more reasonable behaviour of the RF and stacked model, in comparison to the KRR-RBF model, is also evident from the learning curves, where for KRR-RBF we notice an increase of the error on the training set as it gets larger, together with a sudden reduction of the error and variance on the cross-validation set predictions.
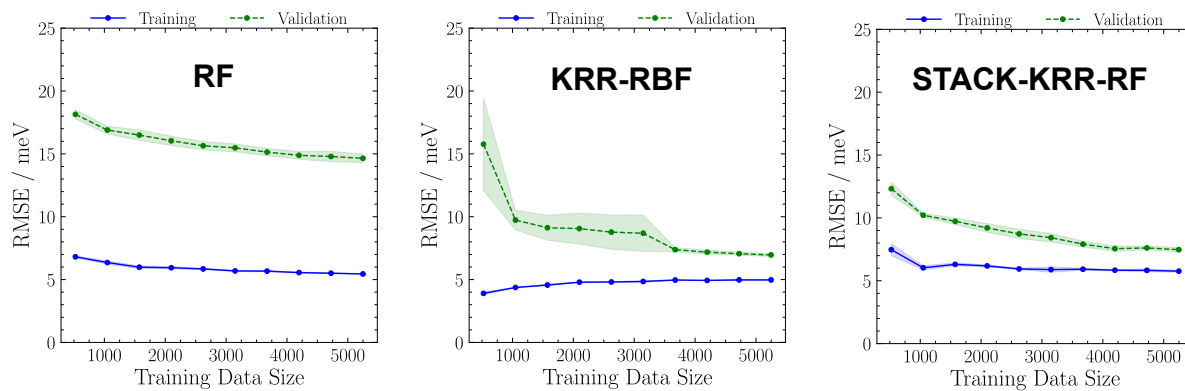
Fig. S4: Learning curves for the best ML models.

S4   Extended Hückel
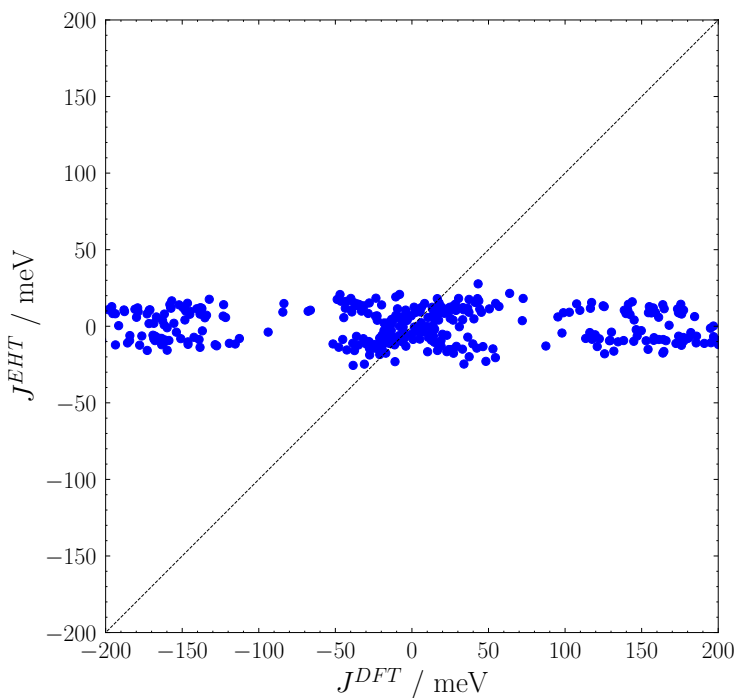
Fig. S5: Comparison between DFT and Extended Hückel transfer integrals.

S5 Spectral density calculations

The spectral density $(S(\omega))$ of the transfer integral J is defined as

$$S(\omega) = \frac{\omega}{k_B T \pi} \int_0^\infty R_i(t) \cos \omega t \, dt \tag{S12}$$

where k_B is the Boltmzann constant, and $R_i(t)$ is the autocorrelation function of the transfer integral J, defined as

$$R_i(t_j) = \frac{1}{N-j} \sum_{k=1}^{N-j} \Delta J_i(t_j + t_k) \Delta J_i(t_k) \tag{S13}$$

$$\Delta J(t) = J(t) - J(0) \tag{S14}$$

which can be computed from the time series of the transfer integral $J(t)$ obtained along a classical MD trajectory. In our case, we computed transfer integrals over 10 ps trajectories, evaluating them every 10 fs, for each value of strain. The spectral densities reported in Fig. 3 in the main text were obtained computing all the autocorrelation functions for each transfer integral J in the simulation box, and then averaging them after grouping according to the transfer integrals type (either J_1 or J_2). Finally, Eq. S12 was applied to these average autocorrelation functions to obtain the spectral densities.

S6 Interaction Networks

A novel point of view on charge transport in organic materials was provided some years ago by Savoie:[54] recognising the analogy between the weighted adjacency matrix, describing the magnitude of connections between vertices of graph, and the electronic Hamiltonian of a molecular aggregate, they analysed charge transport in amorphous aggregates of electron acceptors defining graph descriptors correlating with transport properties.[55] The key point is to compute all electronic interactions between nearest neighbours in the aggregate: they achieved this computa-

tionally intensive task resorting to Extended Hückel Theory. Our ML algorithm enables the same kind of analysis with greater accuracy and speed. In essence, the weighted adjacency matrix $\mathbf{A}$ of a connected graph is replaced with the tight binding electronic Hamiltonian defined as

$$\mathbf{A} = \hat{H} = \sum_i^N E_i \ket{\phi_i}\bra{\phi_i} + \sum_i^N \sum_{j \neq i}^N J_{ij} \ket{\phi_i}\bra{\phi_j} \tag{S15}$$

where specific site energies of the orbitals involved in the transport, E_i, have been usually neglected. A graph is also characterised by two more matrices: the diagonal degree matrix $\mathbf{S}_{ii} = \sum_{i,j} \mathbf{A}_{ij}$, and the laplacian matrix $\mathbf{L} = \mathbf{S} - \mathbf{A}$. Once a graph is defined, it is possible to filter connections between sites by setting an arbitrary threshold J_T, and considering sites i and j connected if $J_{ij} \geq J_T$. Thanks to the availability of all possible transfer integrals along MD trajectories, we computed the electronic interaction network along the trajectories, and analysed the graph obtained by averaging over time. Furthermore, the same authors introduced a descriptor derived from classical resistor theory to characterise charge transport in lattices and amorphous materials.[55] The Moore–Penrose inverse of the laplacian matrix of the graph, $\mathbf{L}^+$, is computed to build the resistance distance matrix $\mathbf{\Omega}_{ij} = \mathbf{L}_{ii}^+ + \mathbf{L}_{jj}^+ - \mathbf{L}_{ij}^+ - \mathbf{L}_{ji}^+$. The charge transport descriptor is named Kirchoff Transport index, defined as

$$K_T = \frac{1}{N^2} \sum_{i,j} \mathbf{\Lambda}_{ij} \tag{S16}$$

$$\mathbf{\Lambda}_{ij} = \begin{cases} 0, & i = j \\ \mathbf{\Omega}_{ij}^{-1}, & i \neq j \end{cases} \tag{S17}$$

where N^2 is a normalisation factor based on the number of sites in the system, and $\mathbf{\Lambda}$ is the admittance distance matrix. K_T describes the resistivity of a network of classical resistors, and in Fig. 4 we report its relative variation (defined similarly to Eq. 3) as a function of mechanical strain ε, also analysing contributions due to each type of transfer integral, *i.e.* building the graph only using J_1 or J_2 transfer integrals.

S23

S7 Kinetic Monte Carlo mobilities

In Table S8 we report the mobilities obtained from kMC simulations used for Fig. 5 of the main manuscript.

Table S8: Hole mobility μ $(\mathrm{cm^2\,V^{-1}\,s^{-1}})$ at different strain evaluated using kMC.

Strain along b		Strain along c	
Strain	μ	Strain	μ
-3%	13.44 ± 0.17	-3%	18.61 ± 0.19
-2%	15.03 ± 0.18	-2%	17.50 ± 0.19
-1%	13.55 ± 0.16	-1%	16.16 ± 0.18
0	13.62 ± 0.16	0	13.62 ± 0.16
$+1\%$	11.90 ± 0.15	$+1\%$	10.72 ± 0.15
$+2\%$	12.30 ± 0.16	$+2\%$	8.32 ± 0.12
$+3\%$	10.51 ± 0.15	$+3\%$	7.26 ± 0.09

References

[1] C. R. Groom, I. J. Bruno, M. P. Lightfoot, S. C. Ward, *Acta Cryst. B* **2016**, *72*, 171–179.

[2] C. Mitsui, T. Okamoto, M. Yamagishi, J. Tsurumi, K. Yoshimoto, K. Nakahara, J. Soeda, Y. Hirose, H. Sato, A. Yamano, T. Uemura, J. Takeya, *Adv. Mater.* **2014**, *26*, 4546–4551.

[3] W. L. Jorgensen, D. S. Maxwell, J. Tirado-Rives, *J. Am. Chem. Soc.* **1996**, *118*, 11225–11236.

[4] C. I. Bayly, P. Cieplak, W. Cornell, P. A. Kollman, *J. Phys. Chem.* **1993**, *97*, 10269–10280.

[5] S. Miertuš, E. Scrocco, J. Tomasi, *Chem. Phys.* **1981**, *55*, 117–129.

[6] M. J. Frisch, G. W. Trucks, H. B. Schlegel, G. E. Scuseria, M. A. Robb, J. R. Cheeseman, G. Scalmani, V. Barone, G. A. Petersson, H. Nakatsuji, X. Li, M. Caricato, A. V. Marenich, J. Bloino, B. G. Janesko, R. Gomperts, B. Mennucci, H. P. Hratchian, J. V. Ortiz, A. F. Izmaylov, J. L. Sonnenberg, D. Williams-Young, F. Ding, F. Lipparini, F. Egidi, J. Goings, B. Peng, A. Petrone, T. Henderson, D. Ranasinghe, V. G. Zakrzewski, J. Gao, N. Rega, G. Zheng, W. Liang, M. Hada, M. Ehara, K. Toyota, R. Fukuda, J. Hasegawa, M. Ishida, T. Nakajima, Y. Honda, O. Kitao, H. Nakai, T. Vreven, K. Throssell, J. A. Montgomery, Jr., J. E. Peralta, F. Ogliaro, M. J. Bearpark, J. J. Heyd, E. N. Brothers, K. N. Kudin, V. N. Staroverov, T. A. Keith, R. Kobayashi, J. Normand, K. Raghavachari, A. P. Rendell, J. C. Burant, S. S. Iyengar, J. Tomasi, M. Cossi, J. M. Millam, M. Klene, C. Adamo, R. Cammi, J. W. Ochterski, R. L. Martin, K. Morokuma, O. Farkas, J. B. Foresman, D. J. Fox, *Gaussian 16 Revision C.01*, **2016**, Gaussian Inc. Wallingford CT.

[7] I. Cacelli, G. Prampolini, *J. Chem. Theory Comput.* **2007**, *3*, 1803–1817.

[8] V. Barone, I. Cacelli, N. De Mitri, D. Licari, S. Monti, G. Prampolini, *Phys. Chem. Chem. Phys.* **2013**, *15*, 3736–51.

[9] J. Cerezo, G. Prampolini, I. Cacelli, *Theor. Chem. Acc.* **2018**, *137*, 80.

[10] A. Landi, D. Padula, *J. Mater. Chem. A* **2021**, *9*, 24849–24856.

[11] L. Greff da Silveira, P. R. Livotto, D. Padula, J. G. Vilhena, G. Prampolini, *J. Chem. Theory Comput.* **2022**, *18*, 6905–6919.

[12] M. J. Abraham, T. Murtola, R. Schulz, S. Páll, J. C. Smith, B. Hess, E. Lindahl, *SoftwareX* **2015**, *1-2*, 19–25.

[13] T. Darden, D. York, L. Pedersen, *J. Chem. Phys.* **1993**, *98*, 10089–10092.

[14] B. Hess, H. Bekker, H. J. C. Berendsen, J. G. E. M. Fraaije, *J. Comput. Chem.* **1997**, *18*, 1463–1472.

[15] H. J. C. Berendsen, J. P. M. Postma, W. F. van Gunsteren, A. DiNola, J. R. Haak, *J. Chem. Phys.* **1984**, *81*, 3684–3690.

[16] G. Bussi, D. Donadio, M. Parrinello, *J. Chem. Phys.* **2007**, *126*, 014101.

[17] F. B. Naughton, I. Alibay, J. Barnoud, E. Barreto-Ojeda, O. Beckstein, C. Bouysset, O. Cohen, R. J. Gowers, H. MacDermott-Opeskin, M. Matta, M. N. Melo, T. Reddy, L. Wang, Y. Zhuang, *Biophys. J.* **2022**, *121*, 272a–273a.

[18] R. Gowers, M. Linke, J. Barnoud, T. Reddy, M. Melo, S. Seyler, J. Domański, D. Dotson, S. Buchoux, I. Kenney, O. Beckstein, *Proceedings of the 15th Python in Science Conference*, **2016**.

[19] N. Michaud-Agrawal, E. J. Denning, T. B. Woolf, O. Beckstein, *J. Comput. Chem.* **2011**, *32*, 2319–2327.

[20] D. L. Theobald, *Acta Crystallogr. Sect. A: Found. Crystallogr.* **2005**, *61*, 478–480.

[21] P. Liu, D. K. Agrafiotis, D. L. Theobald, *J. Comput. Chem.* **2009**, *31*, 1561–1563.

[22] S. Grimme, J. Antony, S. Ehrlich, H. Krieg, *J. Chem. Phys.* **2010**, *132*, 154104.

[23] A. Landi, D. Padula, *J. Mater. Chem. C* **2022**, *10*, 10699–10707.

[24] T. Nematiaram, D. Padula, A. Troisi, *Chem. Mater.* **2021**, *33*, 3368–3378.

[25] A. Troisi, G. Orlandi, *Chem. Phys. Lett.* **2001**, *344*, 509 – 518.

[26] A. Landi, A. Capobianco, A. Peluso, *J. Phys. Chem. Lett.* **2020**, *11*, 7769–7775.

[27] T. Nematiaram, D. Padula, A. Landi, A. Troisi, *Adv. Funct. Mater.* **2020**, *30*, 2001906.

[28] Z.-W. Zhao, Ö. H. Omar, D. Padula, Y. Geng, A. Troisi, *J. Phys. Chem. Lett.* **2021**, *12*, 5009–5015.

[29] G. Zhang, X.-K. Chen, J. Xiao, P. C. Y. Chow, M. Ren, G. Kupgan, X. Jiao, C. C. S. Chan, X. Du, R. Xia, Z. Chen, J. Yuan, Y. Zhang, S. Zhang, Y. Liu, Y. Zou, H. Yan, K. S. Wong, V. Coropceanu, N. Li, C. J. Brabec, J.-L. Bredas, H.-L. Yip, Y. Cao, *Nat Commun* **2020**, *11*, 3943.

[30] A. S. Gertsen, M. K. Sørensen, J. W. Andreasen, *Phys. Rev. Mater.* **2020**, *4*, 075405.

[31] T. F. Harrelson, V. Dantanarayana, X. Xie, C. Koshnick, D. Nai, R. Fair, S. A. Nuñez, A. K. Thomas, T. L. Murrey, M. A. Hickner, J. K. Grey, J. E. Anthony, E. D. Gomez, A. Troisi, R. Faller, A. J. Moulé, *Mater. Horiz.* **2019**, *6*, 182–191.

[32] B. Hourahine, B. Aradi, V. Blum, F. Bonafé, A. Buccheri, C. Camacho, C. Cevallos, M. Y. Deshaye, T. Dumitrică, A. Dominguez, S. Ehlert, M. Elstner, T. van der Heide, J. Hermann, S. Irle, J. J. Kranz, C. Köhler, T. Kowalczyk, T. Kubař, I. S. Lee, V. Lutsker, R. J. Maurer, S. K. Min, I. Mitchell, C. Negre, T. A. Niehaus, A. M. N. Niklasson, A. J. Page, A. Pecchia, G. Penazzi, M. P. Persson, J. Řezáč, C. G. Sánchez, M. Sternberg, M. Stöhr, F. Stuckenberg, A. Tkatchenko, V. W.-z. Yu, T. Frauenheim, *J. Chem. Phys.* **2020**, *152*, 124101.

[33] M. Elstner, D. Porezag, G. Jungnickel, J. Elsner, M. Haugk, T. Frauenheim, S. Suhai, G. Seifert, *Phys. Rev. B* **1998**, *58*, 7260–7268.

[34] M. Gaus, A. Goez, M. Elstner, *J. Chem. Theory Comput.* **2013**, *9*, 338–354.

[35] G. Seifert, J. O. Joswig, *WIREs: Comput. Mol. Sci.* **2012**, *2*, 456–465.

[36] H. J. Monkhorst, J. D. Pack, *Phys. Rev. B* **1976**, *13*, 5188–5192.

[37] A. K. Rappe, C. J. Casewit, K. S. Colwell, W. A. Goddard, W. M. Skiff, *J. Am. Chem. Soc.* **1992**, *114*, 10024–10035.

[38] X. Xie, A. Santana-Bonilla, A. Troisi, *J. Chem. Theory Comput.* **2018**, *14*, 3752–3762.

[39] A. Landi, A. Peluso, A. Troisi, *Adv. Mater.* **2021**, *33*, 2008049.

[40] R. Kubo, Y. Toyozawa, *Prog. Theor. Phys.* **1955**, *13*, 160–182.

[41] M. Lax, *J. Chem. Phys.* **1952**, *20*, 1752–1760.

[42] R. Borrelli, A. Peluso, *WIREs: Comput. Mol. Sci.* **2013**, *3*, 542–559.

[43] R. Borrelli, A. Peluso, *MolFC: A program for Franck-Condon integrals calculation*, Package available online at `http://www.theochem.unisa.it`.

[44] R. Borrelli, M. Di Donato, A. Peluso, *Biophys. J.* **2005**, *89*, 830–841.

[45] S. Fratini, S. Ciuchi, D. Mayou, G. T. De Laissardière, A. Troisi, *Nat. Mater.* **2017**, *16*, 998–1002.

[46] S. Fratini, D. Mayou, S. Ciuchi, *Adv. Funct. Mater.* **2016**, *26*, 2292–2315.

[47] T. Nematiaram, S. Ciuchi, X. Xie, S. Fratini, A. Troisi, *J. Phys. Chem. C* **2019**, *123*, 6989–6997.

[48] J. Lederer, W. Kaiser, A. Mattoni, A. Gagliardi, *Adv. Theory Simul.* **2019**, *2*, 1800136.

[49] F. Pedregosa, G. Varoquaux, A. Gramfort, V. Michel, B. Thirion, O. Grisel, M. Blondel, P. Prettenhofer, R. Weiss, V. Dubourg, J. Vanderplas, A. Passos, D. Cournapeau, M. Brucher, M. Perrot, E. Duchesnay, *J. Mach. Learn. Res.* **2011**, *12*, 2825–2830.

[50] M. Krämer, P. M. Dohmen, W. Xie, D. Holub, A. S. Christensen, M. Elstner, *J. Chem. Theory Comput.* **2020**, *16*, 4061–4070.

[51] C.-I. Wang, M. K. E. Braza, G. C. Claudio, R. B. Nellas, C.-P. Hsu, *J. Phys. Chem. A* **2019**, *123*, 7792–7802.

[52] C.-I. Wang, I. Joanito, C.-F. Lan, C.-P. Hsu, *J. Chem. Phys.* **2020**, *153*, 214113.

[53] V. Coropceanu, J. Cornil, D. A. da Silva Filho, Y. Olivier, R. Silbey, J.-L. Brédas, *Chem. Rev.* **2007**, *107*, 926–952.

[54] B. M. Savoie, K. L. Kohlstedt, N. E. Jackson, L. X. Chen, M. O. de la Cruz, G. C. Schatz, T. J. Marks, M. A. Ratner, *Proc. Natl. Acad. Sci. U.S.A.* **2014**, *111*, 10055–10060.

[55] N. E. Jackson, B. M. Savoie, L. X. Chen, M. A. Ratner, *J. Phys. Chem. Lett.* **2015**, *6*, 1018–1021.